

Multi-objective and multi-fidelity Bayesian optimization of laser-plasma acceleration

F. Irshad,¹ S. Karsch,^{1,2} and A. Döpp^{1,2}

¹*Ludwig-Maximilian-Universität München, Am Coulombwall 1, 85748 Garching, Germany*

²*Max Planck Institut für Quantenoptik, Hans-Kopfermann-Strasse 1, Garching 85748, Germany*

Beam parameter optimization in accelerators involves multiple, sometimes competing objectives. Condensing these multiple objectives into a single objective unavoidably results in bias towards particular outcomes that do not necessarily represent the best possible outcome for the operator in terms of parameter optimization. A more versatile approach is multi-objective optimization, which establishes the trade-off curve or Pareto front between objectives. Here we present first results on multi-objective Bayesian optimization of a simulated laser-plasma accelerator. We find that multi-objective optimization is equal or even superior in performance to its single-objective counterparts, and that it is more resilient to different statistical descriptions of objectives.

As a second major result of our paper, we significantly reduce the computational costs of the optimization by choosing the resolution and box size of the simulations dynamically. This is relevant since even with the use of Bayesian statistics, performing such optimizations on a multi-dimensional search space may require hundreds or thousands of simulations. Our algorithm translates information gained from fast, low-resolution runs with lower fidelity to high-resolution data, thus requiring fewer actual simulations at highest computational cost.

The techniques demonstrated in this paper can be translated to many different use cases, both computational and experimental.

I. INTRODUCTION

Laser-plasma interaction [1, 2] and in particular its sub-field of laser-plasma acceleration [3, 4] are highly researched areas with prospects for numerous scientific and societal applications [5, 6]. Until the past decade, both experimental and numerical investigations in this fields were often based on single or a few laser shots and particle-in-cell simulations [7], respectively. Since then, improvements in laser technology as well as computing hard- and software have made it possible to gather data for hundreds or thousands of different configurations in both experiments and simulations [8–10]. This has sparked interest in using advanced techniques from computer science, in particular machine learning methods, which can deal more efficiently with large data-sets of multi-dimensional data than human operators.

Early examples include the use of genetic algorithms [11, 12] and, more recently, first measurements using surrogate models have been presented [13, 14]. The latter are intermediate models that are generated based on existing data during optimization and that can be quickly explored numerically. Studies involving this *Bayesian* optimization have demonstrated clear optimization of a carefully chosen optimization goal. Importantly, this goal has to be encoded in form of a so-called objective function, which acts on the measurement and gives a scalar output. In the case of a particle accelerator, the beam can generally be described by the charge distribution $\rho(\vec{x}, \vec{p})$ in the six-dimensional phase space and an objective function that optimizes beam parameters will act on this distribution or a subset of it. One of the simplest examples for an objective function is the charge objective function

$$g_Q(\rho(\vec{x}, \vec{p})) = \int \rho(\vec{x}, \vec{p}) d\vec{x} d\vec{p}.$$

While g_Q can, in principle, be used as an objective function in a particle accelerator, it will usually not yield to a useful optimization result. This is because it optimizes *solely* the charge and all other beam parameters such as divergence and energy are lost in the integration process. In fact, due to energy conservation, this optimizer actually tends to reduce the beam energy, which is an unintended consequence in almost all conceivable applications of particle accelerators.

In practice one usually uses a combination of objectives, e.g. reaching a certain charge above a certain energy or the total beam energy. The design of objective functions for these problems is even more difficult, because they need to give some constraints or limits to the single objectives. Many multi-objective scalarizations take the form of a weighted product $g = \prod g_i^{\alpha_i}$ or sum $g = \sum \alpha_i g_i$ of the individual objectives g_i with the hyper-parameter α_i describing its weight. For instance, Jalas *et al.* [14] optimized the spectrum of a laser-accelerated beam using an objective function that combines the beam charge Q , the median energy \tilde{E} and the median absolute deviation $\Delta\tilde{E}$. Their proposed objective function to be maximized is $\sqrt{Q\tilde{E}}/\Delta\tilde{E}$, i.e. the exponential weights are $\alpha_1 = 0.5$, $\alpha_2 = 1$ and $\alpha_3 = -1$. Here, the use of median-based metrics will result in less sensitivity to outliers in the spectrum, while the weight parameter $\alpha_1 = 0.5$ explicitly reduces the relevance of charge compared to beam energy and spread.

The choice of particular weights is, however, entirely empirical and usually the result of trial and error. An objective function is thus not necessarily aligned with the actual optimization goal and one might need to manually adjust parameters of the objective function over multiple optimization runs. In essence, instead of scanning the parameters of an actual experiment or simulation, the human operator will be scanning hyper-parameters of the

objective function.

The underlying problem is that the objective function approach needs to compress a multi-dimensional distribution function into a single number characterizing the distribution. It is impossible to do this lossless for an unknown distribution function. In the case of an unknown one-dimensional distribution function, we can use multiple statistical descriptions to describe the central tendency (weighted arithmetic or truncated mean, the median, mode, percentiles, etc.) and the statistical dispersion of the distribution (full width at half maximum, median absolute deviation, standard deviation, maximum deviation, etc.). These measures weigh different features in the distribution differently. Higher-order features are the skewness, which occurs for instance as a sign of beam loading in energy spectra of laser-plasma accelerators, or coupling terms between the different dimensions. Last, the integral of the distribution function is usually a parameter of interest.[15]

In the following, we will discuss optimizations of electron energy spectra according to different objective definitions and present a more general multi-objective optimization.

The paper is structured as follows: First, we are going to discuss details of the simulated laser-plasma accelerator used for our numerical experiments (Section II). Then we present results from optimization runs using different definitions of scalarized objectives that aim for beams with high charge and low energy spread at a certain target energy (Section III). We then compare these results with an optimization using effective hyper-volume optimization of all objectives (Section IV). In Section V we discuss some of the physics that the optimizer 'discovers' during optimization and in the last section we summarize our results and outline perspectives for future research (Section VI).

II. SYSTEM USED FOR OPTIMIZATION

As a test system for optimization we use an example from the realm of plasma-based acceleration, i.e. a laser wakefield accelerator with electron injection in a sharp density downramp [8, 16]. The basic scenario here is that electrons get trapped in a laser-driven plasma wave due to a local reduction in the plasma density, which is often realized experimentally as transition from one side to the other of a hydrodynamic shock. The amount of electrons injected at this density transition strongly depends on the laser parameters at the moment of injection, but also on the plasma density itself. Both parameters also affect the final energy spectrum the electrons exhibit at the end of the acceleration process. Here we will use simulations to investigate this system, the primary reason being that they are perfectly reproducible and do not require additional handling of jitter, drifts and noise. However, the methods outlined in this paper are equally relevant to experiments. We will restrict the input space to four di-

Input Scan parameters		
Plateau Plasma density	n_e	$min. \ value$ $2 \times 10^{18} \text{ cm}^{-3}$ $max. \ value$ $9 \times 10^{18} \text{ cm}^{-3}$
Upramp length	l_{up}	0.25 mm 1.75 mm
Downramp length	l_{down}	0.0 μm 50 μm
Focus position	z_0	-0.5 mm 2.5 mm
Simulation fidelity	χ	1 4
Input Fixed parameters		
Laser wavelength	λ_0	800 nm
Laser power	P	50 TW
Laser waist (FWHM)	w_0^{FWHM}	20 μm
Laser duration (FWHM)	Δt	30 fs
Dependent variables		
Plasma wavelength	λ_p	$2\pi c\sqrt{m_e\epsilon_0/e^2 n_e}$
Plasma wavenumber	k_p	$2\pi/\lambda_p$
Critical density	n_c	$(2\pi c/\lambda_0)^2 (m_e\epsilon_0/e^2)$
Critical power	P_c	$2m_e c^3 n_c / (r_e n_e)$
Peak intensity	I_0	$2P/(\pi w_0^2)$
Peak potential	a_0	$\sqrt{2I_0/\epsilon_0 c \cdot (e/k_p m_e c^2)}$
Matched peak potential	$a_0^{matched}$	$2(P/P_c)^{1/3}$
Matched bubble radius	r_b	$\sqrt{2a_0^{matched}/k_p}$
Rayleigh length	z_R	$\pi w_0^2/\lambda_0$
Waist	w	$\sqrt{1 + (z - z_0)/z_R}^2$ (Gaussian beam in vacuum)
Simulation mesh parameters		
Transverse box size	l_r	$2.5 \cdot w(z=0)$
Longitudinal box size	l_z	$25 \mu\text{m} + r_b$
Simulation length	$l_{z,max}$	3.5 mm
Transverse resolution	Δr	600 nm/ χ
Longitudinal resolution	Δz	60 nm/ χ
Boost factor	γ_{boost}	$\sqrt{l_{z,max}/l_z}/\chi$

TABLE I. **Simulation and scan parameters.** The top section shows the four simulation parameters and their ranges that are used in the optimization problem. Furthermore, a fidelity parameter χ is introduced that allows the optimizer to choose between low and high numerical resolution (see section on mesh parameters). Based on the scan parameters and the fixed problem parameters, we calculate a number of dependent variables that help us to estimate the correct box size for the simulations.

mensions, comprising of the the plateau plasma density, position of laser focus, as well as the lengths of the up- and downramps of the plasma density close to the density transition.

The shock injection scenario is sufficiently complex to require particle-in-cell codes, but at the same time we can use optimized simulations to achieve a run-time of just a few GPU minutes per simulation, thus enabling us to perform on the order of a thousand simulations per day on a small computing cluster. To achieve this we use the code FBPIC by Lehe et al.[17], which includes several features that significantly reduce the necessary run-time of each simulations. On the hardware side the code is optimized to run on GPUs. Optimization regarding the physical model include usage of a cylindrical geometry with Fourier decomposition in the angular direction and boosted-frame moving windows [18]. Additionally,

we can take advantage of the very localized injection to locally increase the macro-particles density in the injection area [8]. Similarly, the linear wakefields forming in regions of lower laser intensity results in a nearly laminar flow of particles, meaning that we can decrease the macro-particle density far away from the laser axis. [19].

One particular challenge that arises in simulations over a large range of parameters is that different input parameters may have different computation requirements. For instance, the transverse box size needs to be several times larger than the beam waist, so that the energy of a focusing beam is not lost. Hence, a laser that is initialized out of focus requires a larger box size than a beam initialized in focus. We address this by initializing the transverse box size l_r as a function of the laser waist $w(z)$ at the beginning of the simulation. Similarly, the size of the wakefield depends on the plasma density and accordingly, we scale the longitudinal size l_z of the box with the estimated wakefield size. Using these adapted grid sizes, we avoid wasting computational resources and only capture the physics relevant to our problem. It should be noted that the scan range of these highly optimized simulations is limited by the appearance of numerical instabilities or artifacts at e.g. very high plasma density.

Despite these numerous optimizations, running a simulation with sufficiently high resolution that the results for each optimization goal converge numerically still takes several GPU hours. To further speedup the optimization process and allow for multi-dimensional optimization, we make use of low-resolution simulations that capture the essential physics of injection and acceleration, but are not yet fully converged in terms of final charge, energy and so forth. These approximate solutions take only a few GPU minutes to compute, while providing valuable guidance for optimization. Importantly, we can directly incorporate the possibility of varying the *fidelity* of a simulation into the optimization process by introducing a new fidelity variable χ . In a process called multi-fidelity optimization, we construct a Gaussian process that models the objective function over the four input dimensions $(n_e, l_{up}, l_{down}, z_0)$ as well as the fidelity parameter χ . The decision regarding the next position to probe is taken by our recently introduced multi-fidelity, multi-objective Bayesian optimization algorithm [20], which is based on the common optimization of the different objectives and an additional trust objective. Regarding the latter, the algorithm also takes into account the computational cost associated with the fidelity parameter, which in our case is roughly scaling with $cost(\chi) \propto \chi^{3.5}$. The speed up gained by taking this cost and fidelity information into account is on average an order of magnitude in this study. This is considering the time taken by the scalarized single-objective functions to yield the optimized spectrum and not the total time of the optimization. A summary of all free and dependent parameters of the simulations is given in Table I.

Objective definitions	
Objective 1	O_1 $Q^{0.5}((\epsilon + \Delta\bar{E}^2)\sigma_E)^{-1}$, Eq. (1)
Objective 2	O_2 $Q^{0.5}((\epsilon + \Delta\tilde{E})E_{MAD})^{-1}$, Eq. (2)
Objective 2 _a	O_{2a} $Q^2((\epsilon + \Delta\tilde{E})E_{MAD})^{-1}$, Eq. (4)
Objective 2 _b	O_{2b} $Q^3((\epsilon + \Delta\tilde{E})E_{MAD})^{-1}$, Eq. (5)
Objective 3	O_3 $2Q_{in} - Q$, Eq. (3)

Charge-related metrics	
Q	Total integrated charge
Q_{in}	Charge within an energy interval $E_0 \pm \Delta E$

Central tendency metrics	
\bar{E}	Mean energy
\tilde{E}	Median energy
E_0	Target energy (300 MeV)
$\Delta\bar{E}^2$	Mean-squared difference of median and target energy
$ \Delta\tilde{E} $	Absolute difference of median and target energy

Statistical dispersion metrics	
σ_E	standard deviation
E_{MAD}	median absolute deviation

TABLE II. **Summary of single-objective functions used in the paper.** The five single-objective scalarized functions that are optimized in this study are shown at the top. The middle and bottom half shows the charge, central tendency and statistical dispersion metrics used to construct the single-objectives. These are also used in the multi-objective multi-fidelity optimization.

III. SINGLE-OBJECTIVE, MULTI-FIDELITY OPTIMIZATION

The goal of the optimization presented here is to produce quasi-monoenergetic electron beams with high charge around a certain target energy E_0 . In statistical terms these goals can be captured by the difference of the central tendency from the target energy, statistical dispersion and the integral of the electron beam spectrum. But as mentioned in the introduction, these three features can be described by multiple statistical measures such as the standard deviation, median absolute deviation, mean energy, median energy and total charge [21]. We also include the normalized fidelity $(\chi - 1)/3$ as another input parameter, which dictates the resolution of the simulation that can be dynamically chosen by the algorithm, cf. Table I. This makes the optimization a $(n_{input} \times n_{obj}) = (5 \times 1)$ dimensional problem where the multiple output objectives are condensed into a single objective function. A summary of these single-objective functions and definitions of metrics used for the electron beams is outlined in Table II. All the input parameters are scaled to lie within a unit hypercube $[0, 1]^5$. All methods described in this manuscript are, however, valid for an arbitrary number of input dimensions.

In this section we will discuss four different scalarized objectives that arise from different combinations of statistical descriptors for the targeted spectral distribution,

namely the integral, the central tendency and the statistical dispersion. All of these objectives intend to capture the same general objective, i.e. simultaneously maximize charge, reduce spectral width and reduce distance to the target energy. However, as we will show in the following, differences in calculating and weighing each of these individual objectives lead to significant differences in the final optimization result.

Examples. In terms of the mean energy and standard deviation we can for instance define the objective:

$$O_1 = Q((\epsilon + \Delta\bar{E}^2)\sigma_E)^{-1} \quad (1)$$

where Q is the total charge, $\Delta\bar{E}^2 = |\bar{E} - E_0|^2$ is the squared difference between the mean energy \bar{E} of the spectrum and the target energy, and σ_E is the standard deviation. The factor ϵ is an offset to prevent the objective from approaching infinity as the distance to the target energy is decreased. Throughout the manuscript we use $\epsilon = 1$ MeV, as beams within a distance of 1 MeV to the target energy are considered sufficiently optimized.

It is a characteristic of the mean that it (over-)emphasises points further away from the target. In presence of noise it is thus often suitable to use median-based descriptors, instead. Such an objective could be

$$O_2 = Q^{0.5}((\epsilon + |\Delta\tilde{E}|)E_{MAD})^{-1}, \quad (2)$$

where Q is the total charge, \tilde{E} is the median energy of the spectrum, E_0 is the target energy, $|\Delta\tilde{E}| = |\tilde{E} - E_0|$ —is their absolute distance and E_{MAD} is the median absolute deviation around median. The square root in the objective aims to decrease the emphasis placed on the total charge. This is essentially the aforementioned objective used in Jalas et al., with the difference that we use a target energy instead of an energy maximization [14].

A general problem of defining objectives in terms of division previously alluded to, is that they could be arbitrarily increased by decreasing the value given in the denominator. For the study of [14] this particular objective still works because the optimization goal is to achieve maximum energies but it can lead to sub-optimal beams when optimizing to a fixed target energy.

As an alternative to the concepts of central tendency and statistical dispersion, we can try to implement the optimization goals as optimization of the charge within a certain energy window. This can for instance be done using the form

$$O_3 = 2Q_{in} - Q, \quad (3)$$

where $Q_{in} = \int_{E_0 - \Delta E/2}^{E_0 + \Delta E/2} Q(E)dE$ is the charge within an given energy interval ΔE around the target energy. As mentioned in the preceding paragraph, it is important to implement this concept without division. For instance, it would seem that an objective $O_4 = Q_{in} \cdot (Q - Q_{in})^{-1}$ would be more or less equivalent to optimize, yet here the objective value can be arbitrarily increased by reducing

Optimization parameters		
Number of Trials	n_{TRIALS}	5
Number of Iterations	n_{BATCH}	150
Total Cost	C_{total}	4500 (50 GPU hours)
Number of initial points	n_{INIT}	5
Input Dimensions	dim_x	5
Output Dimensions	dim_y	1 and 3 (MOMF)
Cost Function	$cost(\chi)$	$\chi^{3.5}$

TABLE III. **Summary of optimization parameters used in the paper** Some of the parameters used to run the MOMF algorithm are outlined in this table. The number of iterations and total cost are two upper thresholds used to stop the optimization run. When either values were reached the optimization was stopped. The output dimensions for scalarized runs was 1 while the MOMF optimized 3 objectives simultaneously. The cost function is an approximated due to the adaptive meshes used in this study.

the charge outside of the desired energy interval towards zero. Indeed, optimization tends to produce beams with near-zero charge. Meanwhile, the additive version Eq. (3) does not suffer from this issue and, as we will discuss in the following, leads to good optimization results despite its simplicity.

Optimization. The three above objectives were used to optimize the simulated laser wakefield accelerator with the goal of achieving beams close to the target energy. For optimization we use Bayesian optimization (BO) based on Gaussian Process Regression (GPR). The regression inputs in this study are the laser and plasma parameters of FBPIC simulations and the output of the GPR is the single objective functions after acting on the FBPIC output beams. The basis of BO is modelling the Laser Wakefield Accelerator (LWFA) using GPR and constructing an acquisition function using the GPR mean and variance. This acquisition function indicates positions where the GPR predictions yield a better value for the objective function. The input parameters that maximizes the acquisition function are used as the input to the LWFA. After evaluating the LWFA using FBPIC simulations, the objective values are fed back into the model and the acquisition function constructed again. In this work all Bayesian optimizations use a novel acquisition function for simultaneous multi-fidelity, multi-objective optimization [20], which facilitates comparison to results in Section IV. While designed for multiple objectives, the acquisition function also supports optimization of a single objective LWFA with multiple fidelities, which reduces the optimization time. All the single-objective optimization were executed 5 times with 5 random initial points. The run that achieved the highest objective value was selected as the trial to compare with the MOMF for each of the single objectives. The different optimization parameters used for the single and multi-objective runs is outlined in Table III.

The total computational budget for each run was kept to 50 GPU hours or 150 iterations whichever was reached

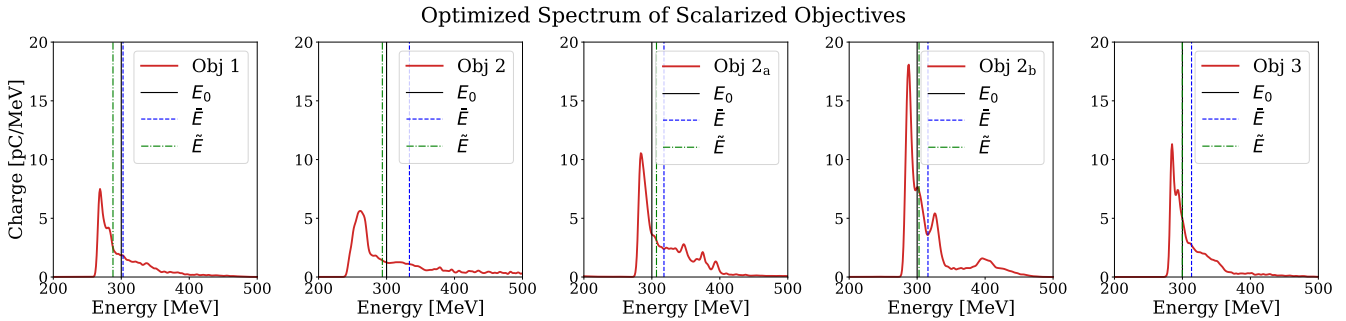


FIG. 1. **Single-objective spectra.** Final, optimized spectrum for three different scalarizations of beam charge, beam distance from target energy and beam width. The solid black line denotes the position of the target energy 300 MeV, while the blue and green dashed lines represent the mean and median energy for each spectrum. The third objective specifically optimizes for higher charge within the 250-350 MeV range. This results in a beam with a much higher charged beam while also having a mean energy close to the target energy.

earlier. When comparing the optimization runs, the time taken to reach the optimized result was taken into account. For objective 1 this time was about 280 while objectives 2 and 3 took about 13.3 GPU hours. In Section IV the multi-objective is also compared with the single-objective runs in terms of run-time and optimized solutions.

In Figure 1, we show the final spectrum of three scalarized objectives. Since we use mean energy for the first objective the spectrum outliers can influence the mean much more than the second objective using median energy. This is why the first spectrum tends to not have any high or low energy tail. The second spectrum using median energy and median absolute deviation allows having high energy tail while keeping the median close to 300 MeV. Since this spectrum has a longer tail the mean of this spectrum is higher than 300 MeV. The third objective shown at the very right in Figure 1 has a much higher charge peak charge because it has a higher implicit weighting on charge. The beam here has even a shorter tail since it explicitly penalizes charge outside of the 250-350 MeV window. Overall we can see that the different scalarization of the statistical measures can result in different spectra. Also, implicitly optimizing for beams near a target energy as is done in the case of objective 3 can result in beams which are better than explicitly optimizing for it.

Influence of Hyper-parameters. Having seen the solutions from optimizing the three different objectives, we now illustrate the effect of changing the hyper-parameters of the scalarized objective. To achieve this, the hyper-parameters of the second objective Eq. (2) were modified by changing the exponent of charge yielding the following two objectives

$$O_{2,a} = Q^2((\epsilon + |\Delta \tilde{E}|)E_{MAD})^{-1}, \quad (4)$$

$$O_{2,b} = Q^3((\epsilon + |\Delta \tilde{E}|)E_{MAD})^{-1}. \quad (5)$$

Here the power of the total charge was changed from 0.5 to 2 and 3. We can see the changes this makes on the optimal solution in Figure 1. Going from an exponent of 0.5 to 2 increases the total charge in the optimized beam spectrum. As one would expect, when we increase the hyper-parameter of charge from 2 to 3, the total beam charge increases even further. The time taken for this optimization was 6 and 10.8 GPU hours for objectives 2a and 2b respectively. We can see that the optimized spectrum in this case is also better in terms of the energy bandwidth and distance to target energy, even though these hyper-parameters were not changed. However, while this particular combination of hyper-parameters appears to yield objectively better beams than other variations O_2 and O_{2a} , it is not possible to know this beforehand, adding the hyper-parameter choice as an additional degree of freedom to the optimization problem.

IV. MULTI-OBJECTIVE, MULTI-FIDELITY OPTIMIZATION

As we have seen in the previous section, a major problem with the single-objective optimizations of complex systems is that the weights for the hyper-parameters of the scalarization model are entirely empirical. To get a higher value for one particular objective, the weights need to be changed via trial and error. This usually also changes the other objectives, which can be either detrimental or advantageous giving less control to the end user. Furthermore, multi-objective optimization problems often exhibit some trade-off in the optimization of different objectives. A single-objective optimization will always be biased towards one particular trade-off, which might not be the optimal trade-off for the actual application.

A more versatile strategy is to directly explore the trade-off between different objectives and then choose the optimal combination of objectives that result in the best

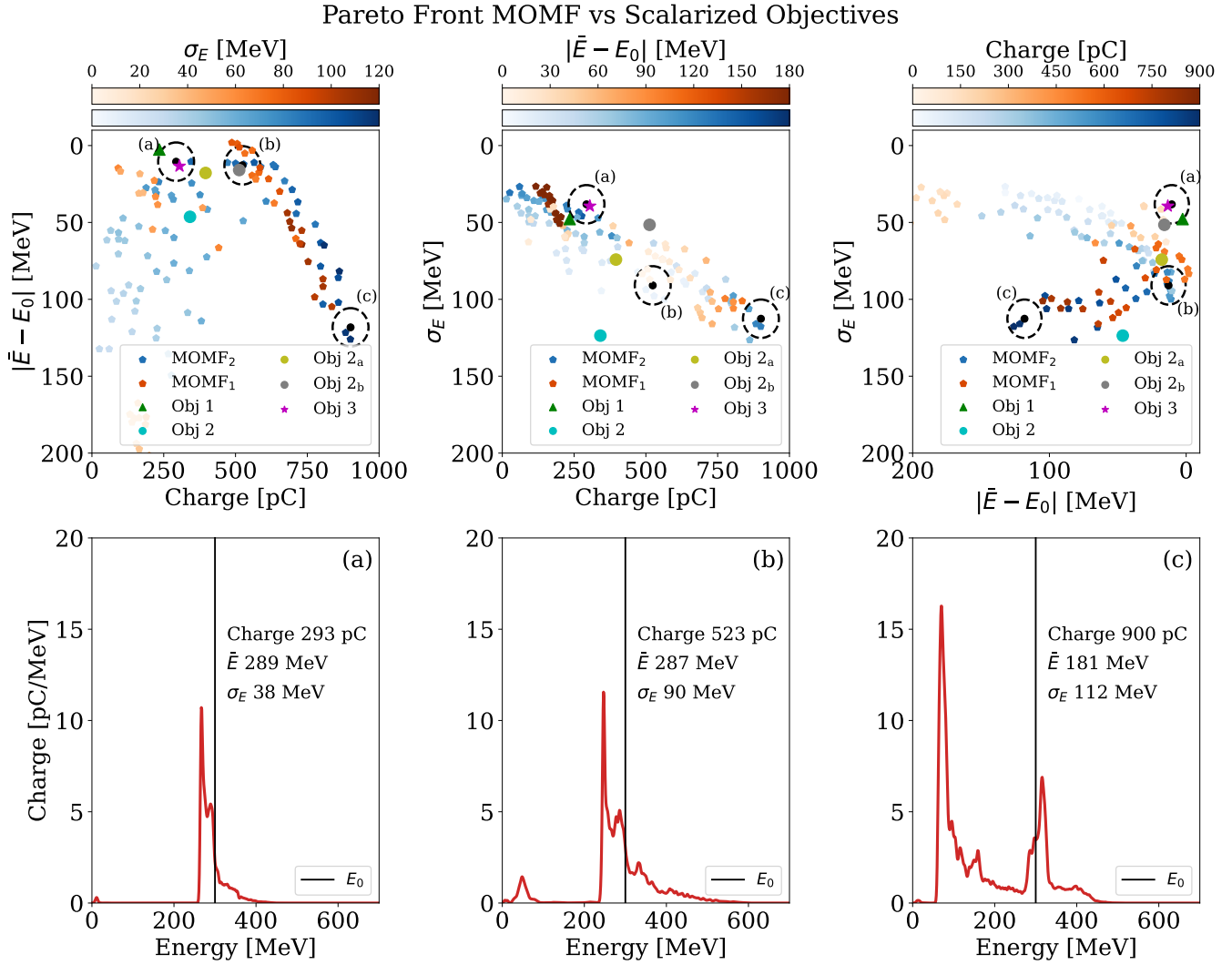


FIG. 2. 3D-Pareto front MOMF. This figure shows the results of the MOMF optimization in the form of a Pareto front. The three objectives shown in the three subplots at the top are the distance of the mean energy from target energy, standard deviation of the beam and the total charge. The top three sub-figures depict projections of the 3D Pareto front onto these three objectives, with the missing objective color-coded according to the attached color-maps. In each of the projections the best potential point would be situated on the top right maximizing both objectives. The three scalarized objectives along with the objectives with various hyper-parameters are also shown in the 2D projections. This graph also shows the results of MOMF optimization using different statistical measures. MOMF₁ is the optimization using the median energy and median absolute deviation while MOMF₂ is optimization using mean energy and the standard deviation. We can see from the plot that the MOMF₁ and MOMF₂ optimizations yield points close to each on the 3D Pareto surface. The MOMF has points spanning a large volume of the Pareto front. The bottom part shows the spectrum of 3 points labelled a,b,c taken from the MOMF₂ optimization that are highlighted in the top part in black with circles. We can see how the spectra in different parts of the Pareto surface differ while still having a reasonable amount of charge around the target energy. This choice of having different spectra that can be generated in a single MOMF optimization run is a significant advantage over the single-objective optimization.

trade-off. This trade-off optimization results in a solution set that in the output space is known as the Pareto front and in the input space as Pareto set. A point is said to dominate another when it has at a minimum higher value for one objective keeping others equal. Thus the Pareto front is the set of non-dominated points in any given output space. The area covered by the dominated space is known as the hyper-volume and it measures the quality of the Pareto front. The expected improvement in hyper-volume by evaluating a point is the basic metric which is used to optimize different objectives. This algorithm can be adapted in the multi-fidelity setting by weighting the expected improvement in hyper-volume with the cost of a simulation.

This algorithm known as Multi-objective Multi-fidelity optimization (MOMF) [20] can optimize several objectives along with a trust objective that rewards higher fidelity simulations. The beam parameters optimized using MOMF were the mean energy difference $|\bar{E} - E_0|$, standard deviation σ_E and total charge in the beam Q .

Results. In Fig. 2 we show the result of the MOMF optimization that yields a 3D Pareto front consisting of all the non-dominated points. This figure shows some trade-offs that can be explained physically. One of the prominent features can be seen in the left plot where an increase in the distance to target energy is seen when the total charge exceeds 600 pC. This distance is mainly a decrease in energy which is a characteristic of beam loading [8]: As the charge increases the electron bunch modifies the wakefields, which consequently leads to lower mean energy and an increase in the distance to the target energy. Another trade-off in the center plot between high charge and mono-energetic beams is seen whereby increasing charge results in a wider spectrum of the electron beams. This indicates that the input parameters that yield a beam with a higher total charge are different from the ones that produce quasi-mono-energetic beams. Another interesting result in this optimization run was the absence of any high energy beams with low charge. This is because high-energy beams are implicitly excluded by the three objectives. As the energy increases, the distance to the target energy increased and the charge injected for these high energy beams is less than those for lower energy beams. Hence, the beams majorly were restricted to near target or lower than target energy.

The effect of exploring inherent trade-offs makes MOMF a powerful technique. The benefits are two-fold since on one hand the MOMF could be used to characterize the capability of the accelerator in optimizing each objective while on the other hand it can yield multiple results that a user can choose without running multiple optimization loops. MOMF optimization also avoids the problem seen in single-objective where increasing the distance to the target energy yielded highest scalarized objective values. The MOMF does not benefit from optimizing a single objective since it tries to take points that increase the hyper-volume significantly. These are the points that can result in higher values for multi-

ple objectives. Hence exploiting a single objective in the MOMF optimization is avoided. The figure shows that the MOMF gives a complete set of solutions spanning a large portion of the Pareto front while the single-objective scalarized optimization covers only a small part of this 3D space. Moreover, all of the single-objective points with the exception of objective 3 and objective 2b, which was tuned by its hyper-parameters, are dominated by the points generated using MOMF optimization.

Runtime comparison. The optimization run-time to generate the optimized point from objective 3 took 13.6 GPU hours as opposed to 10 GPU hours that took the MOMF to produce the solution set seen here. In this study, the single-objective run-times ranged from 4 to 13.5 GPU hours for a single optimization run. The MOMF run-times were within this range while yielding multiple solutions and being robust against variation in statistical measures used. Moreover, if this study was undertaken using only the highest fidelity the run-times for single-optimization would range from 33 to 100 GPU hours. Thus we reduce the run-times by an order of magnitude at best and by a factor of 8 at worse by dynamically choosing resolution of simulations. If the hyper-parameters of the single-objective are tuned, they result in even longer run-times than the MOMF.

All of the MOMF points in this figure are generated using the Gaussian process with the exception of points in black which are actual FBPIC simulations whose spectra are also shown in the bottom half of Fig. 2. Spectra (a) and (b) show a similar distance to the target energy but exhibit a charge and statistical dispersion trade off. It is quite subjective as to which of the spectra are better hence the MOMF provides both as a solution among which the user is free to decide. In Table IV we also present a summary of all the results obtained in this study with MOMF and different single-objectives. We can see that the spectra of the MOMF_b and Obj 2_b are objectively better if defined in terms of total charge, mean energy and standard deviation. Other spectra can also be subjectively very close to each other, as already discussed before.

Robustness to variation in statistical measures. We previously showed how scalarization is sensitive with respect to the statistical measures used. This was visualized in cf. Fig. 1, where we got differing spectra at the end of optimization depending on the statistical measures used to describe the electron beams. In contrast, the multi-objective optimization is more robust regarding the use of various statistical measures. This can be attributed to the more exploratory nature of the multi-objective optimization. Here we show results from two different optimizations where we used median energy and median absolute deviation for MOMF_1 while using mean energy and standard deviation for MOMF_2 to describe electron beams. The results at the end are transferred to one common space comprising of mean energy and standard deviation. As shown in Fig. 2, the Pareto fronts derived using a MOMF_1 optimizer (in red) and MOMF_2

Summary of MOMF and Single-objective results								
	MOMF _a)	MOMF _b)	MOMF _c)	Obj 1	Obj 2	Obj 2 _a)	Obj 2 _b)	Obj 3
Total Charge (pC)	293	523	900	235	339	396	513	305
Mean Energy (MeV)	289	287	181	303	334	318	316	313
Standard Deviation (MeV)	38	90	112	48	104	74	52	39

TABLE IV. **Summary of MOMF and Single-Objective results** This table summarizes the results of the MOMF and single-objective optimizations. MOMF_a), MOMF_b) and MOMF_c) are the three chosen points from the MOMF₂ solution set as shown in Fig. 2. We can see that the best two spectra are the ones from MOMF_b) and from hyper-parameter optimized Obj 2_b).

optimizer (in blue) are very similar.

V. INPUT SPACE ANALYSIS

In this section we will take a look at the input space to understand how the various physical parameters influenced the objective values. This also provides an insight into how the algorithm was able to find spectra spanning a wide range of the Pareto front. The data from the different trial runs for the MOMF₂ objectives was used to train a GP model. This trained GP model was then probed with 4096 points with their fidelity parameter fixed at the highest fidelity. The GP then returns a mean value of the three different objectives at each position of the test points. This data can be used to generate plots that map the influence of the input parameters on the individual objectives. For this the data is binned by taking pair-wise input parameters while averaging over the other two. This results in a total of 6 2D plots for 4 input parameters which are color coded by the values of the output objective. We can also see the influence of a single parameter by repeating the same procedure as above by averaging over the three input parameters. This is repeated three times to generate plots that are color-coded for each output objective.

The results are shown in Figure 3. The red color in all the graphs denotes the optimized values for each objective where charge was maximized while the distance to the target energy and the statistical dispersion are being minimized. We can observe some physically interpretable trends that the optimizer can use to generate beams along the Pareto front.

- The influence of density can be analyzed keeping the goal of the optimization in perspective. Since the optimization goal was to keep the energy fixed at 300 MeV a lower density would reduce the charge injected and consequently result in negligible beam loading resulting in greater wake-field strength. This in turn would yield a higher energy of the electron beam that results in an increased distance. If the density is increased beyond the optimum it would result in beam loading effect as seen earlier in 2 that would result in flattening of the fields and hence a reduced beam energy that also results in a greater distance [8]. Thus there is an optimum density dip that is seen for optimizing the distance to the target energy.
- The distance to the target energy is minimized for a specific value of focus and plateau density. Such specific values indicate that the injected electrons have a certain acceleration length required to reach an energy of 300 MeV without overshooting.
- As expected, the length of the downramp directly affects the injected charge, with shorter downramps corresponding to a more rapid wakefield expansion and thus increased injection. Meanwhile, the downramp length shows no influence on the mean energy, which also is to be expected because within the ranges scanned here it controls the point of the injection and not the acceleration length.
- The energy spread also shows specific values of density and focus that are achieved for optimal energy spread. However, it is difficult to evaluate trends due to the strongly coupled influence of input parameters on the energy spread. A specific focus value can result in a localized point of injection that also needs specific values of upramp and density to result in optimal beam loading resulting in flat phase space. However, a linear trend in 2D plot of upramp and focus show an almost constant energy spread that is due to the fact that when the up ramp length is increased the density transition is translated deeper into the plasma. This in turn requires the focus parameter to be increased to generate higher intensities near the density transition that ultimately yields a lower energy spread value. the most optimized values of energy spread require an earlier focus.
- We observe that the injected charge increases linearly with the upramp length. This effect is most likely related to laser self-focusing, where a longer upramp allows for stronger self-focusing of the laser and hence, a higher laser intensity at the injection point.
- A last observation is that the total charge is not monotonically increasing with density as one might expect. Upon closer inspection, we observed that

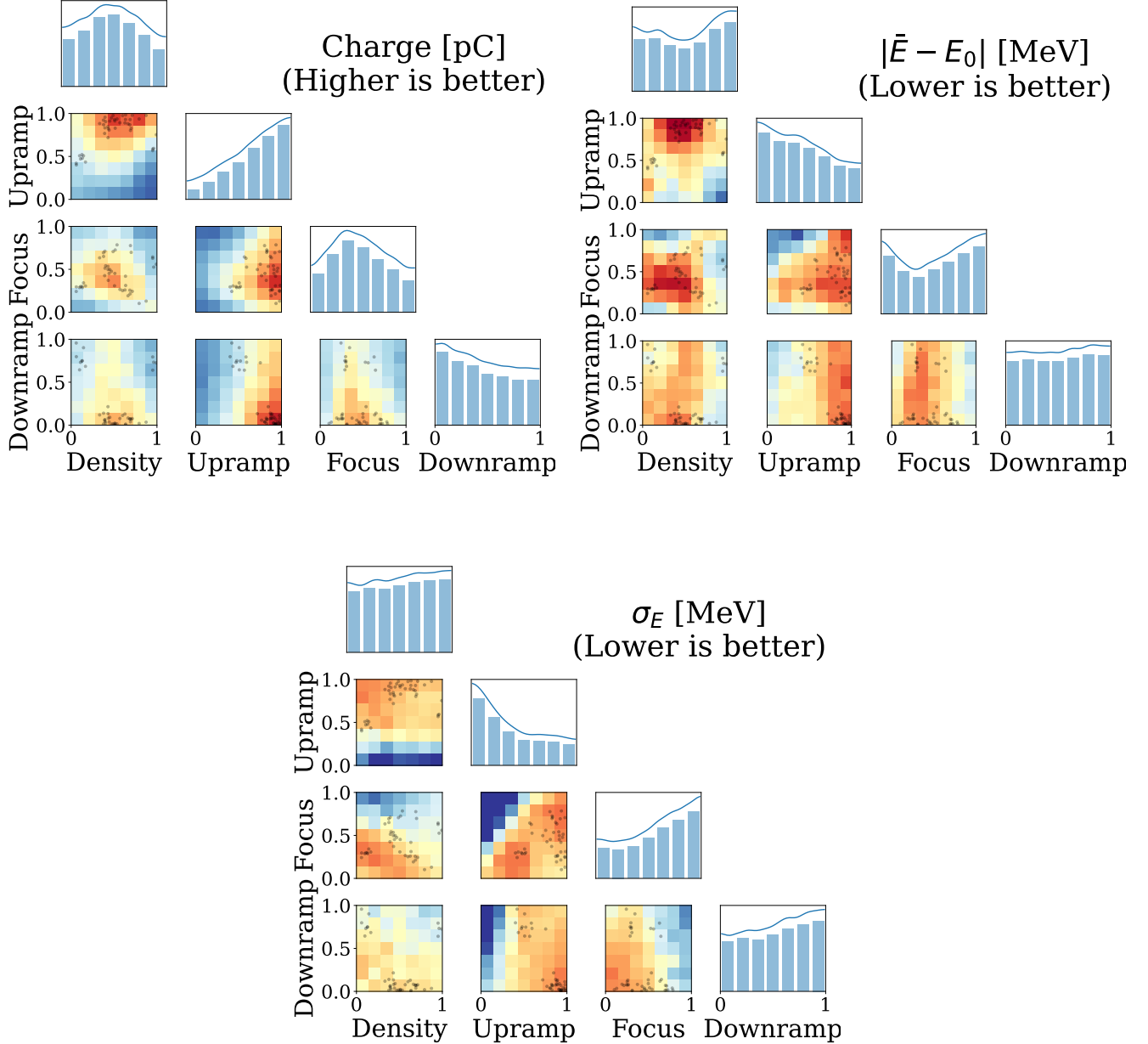


FIG. 3. 4D-Input Space. This figure shows the averaged effect of the input parameters on the three objectives that were optimized in the multi-objective optimization. The four input parameters shown in the figure are the plasma density, up ramp length, down ramp length and the focus position of laser pulse. The top left part shows the effect of each of these input parameters on charge, the top right part shows the effect on the distance of the mean to the target energy and the bottom part shows the effect on the standard deviation. In each part, the 1D histograms show an averaged effect of one input on the output in that part. In all of the parts the red color denotes optimized values for each objective. Also shown in all of the plots are the points that make up the Pareto front of MOMF₁ in Figure 2. This shows how the MOMF algorithm clustered around regions in the input space that yield optimized objective.

the injected charge indeed increased, however the final beam charge is reduced due to dephasing and defocusing of parts of the electrons.

VI. CONCLUSION AND OUTLOOK

To conclude, we have presented first multi-objective optimization of a simulated laser-plasma accelerator. The performance of the multi-objective optimizer was benchmarked against several single-objective optimizers and it was found to lead to at least equal, but often superior results. Meanwhile, the multi-objective optimizer yields a far more general result that does not require iterative fine-tuning of objective parameters.

By combining a state-of-the-art GPU-based simulation code with a multi-fidelity optimization algorithm, we were able to perform extensive, multi-dimensional optimizations that are to our knowledge without precedent in the field of notoriously expensive particle-in-cell simulations of physical systems. This results is a milestone towards using 'digital twins' of complex physical systems to optimize real-life experiments and infrastructure. This does not only concern laser-plasma acceleration, but ap-

plies to any optimization problem with different available numerical resolution.

While the multi-fidelity component most immediately benefits simulation studies with different resolution, the multi-objective techniques presented in this paper can also be directly transferred to experiments. As already noted by [13] and discussed in Section V, surrogate models carry significant information about the physics interaction that can help physicists to better understand couplings between input and output parameters. This information may directly be used to improve experiments, e.g. as a prior for Bayesian optimization in experiments.

ACKNOWLEDGMENTS

This work was supported by the DFG through the Cluster of Excellence Munich-Centre for Advanced Photonics (MAP EXC 158), TR-18 funding schemes and the Max Planck Society. It was also supported by the Independent Junior Research Group "Characterization and control of high-intensity laser pulses for particle acceleration", DFG Project No. 453619281. F.I. is part of the Max Planck School of Photonics supported by BMBF, Max Planck Society, and Fraunhofer Society.

[1] A. Macchi, M. Borghesi, and M. Passoni, Ion acceleration by superintense laser-plasma interaction, *Reviews of Modern Physics* **85**, 751 (2013), 1302.1775.

[2] P. McKenna, D. Neely, R. Bingham, and D. Jaroszynski, eds., *Laser-Plasma Interactions and Applications*, Scottish Graduate Series, Vol. 1 (Springer, Heidelberg, 2013).

[3] E. Esarey, C. B. Schroeder, and W. P. Leemans, Physics of laser-driven plasma-based electron accelerators, *Reviews of Modern Physics* **81**, 1229 (2009).

[4] J. Wenz and S. Karsch, Physics of Laser-Wakefield Accelerators (LWFA), arXiv 10.48550/arXiv.2007.04622 (2020), 2007.04622.

[5] F. Albert and A. G. R. Thomas, Applications of laser wakefield accelerator-based light sources, *Plasma Physics and Controlled Fusion* **58**, 103001 (2016).

[6] P. Bolton, K. Parodi, and J. Schreiber, *Applications of laser-driven particle acceleration* (CRC Press, 2018).

[7] V. Malka, Laser plasma accelerators, *Physics of Plasmas* **19**, 055501 (2012).

[8] J. Götzfried, A. Döpp, M. F. Gilljohann, F. M. Foerster, H. Ding, S. Schindler, G. Schilling, A. Buck, L. Veisz, and S. Karsch, Physics of High-Charge Electron Beams in Laser-Plasma Wakefields, *Physical Review X* **10**, 041015 (2020), 2004.10310.

[9] M. Kirchen, S. Jalas, P. Messner, P. Winkler, T. Eichner, L. Hübner, T. Hülzenbusch, L. Jeppe, T. Parikh, M. Schnepp, and A. R. Maier, Optimal Beam Loading in a Laser-Plasma Accelerator, *Physical Review Letters* **126**, 174801 (2021).

[10] S. Bohlen, J. C. Wood, T. Brümmmer, F. Grüner, C. A. Lindström, M. Meisel, T. Staufer, R. D'Arcy, K. Pöder, and J. Osterhoff, Stability of ionization-injection-based laser-plasma accelerators, *Physical Review Accelerators and Beams* **25**, 031301 (2022), 2203.00561.

[11] Z.-H. He, B. Hou, V. Lebailly, J. Nees, K. Krushelnick, and A. Thomas, Coherent control of plasma dynamics, *Nature Communications* **6**, 7156 (2015), 1501.04117.

[12] M. J. V. Streeter, S. J. D. Dann, J. D. E. Scott, C. D. Baird, C. D. Murphy, S. Eardley, R. A. Smith, S. Rozario, J.-N. Gruse, S. P. D. Mangles, Z. Najmudin, S. Tata, M. Krishnamurthy, S. V. Rahul, D. Hazra, P. Pourmousavi, J. Osterhoff, J. Hah, N. Bourgeois, C. Thornton, C. D. Gregory, C. J. Hooker, O. Chekhlov, S. J. Hawkes, B. Parry, V. A. Marshall, Y. Tang, E. Springate, P. P. Rajeev, A. G. R. Thomas, and D. R. Symes, Temporal feedback control of high-intensity laser pulses to optimize ultrafast heating of atomic clusters, *Applied Physics Letters* **112**, 244101 (2018), 1804.07488.

[13] R. J. Shalloo, S. J. D. Dann, J.-N. Gruse, C. I. D. Underwood, A. F. Antoine, C. Arran, M. Backhouse, C. D. Baird, M. D. Balcazar, N. Bourgeois, J. A. Cardarelli, P. Hatfield, J. Kang, K. Krushelnick, S. P. D. Mangles, C. D. Murphy, N. Lu, J. Osterhoff, K. Pöder, P. P. Rajeev, C. P. Ridgers, S. Rozario, M. P. Selwood, A. J. Shahani, D. R. Symes, A. G. R. Thomas, C. Thornton, Z. Najmudin, and M. J. V. Streeter, Automation and control of laser wakefield accelerators using Bayesian optimization, *Nature Communications* **11**, 6355 (2020), 2007.14340.

[14] S. Jalas, M. Kirchen, P. Messner, P. Winkler, L. Hübner, J. Dirkwinkel, M. Schnepp, R. Lehe, and A. R. Maier, Bayesian Optimization of a Laser-Plasma Accelerator, *Physical Review Letters* **126**, 104801 (2021).

[15] One 'exception' may be applications that deal with probability distributions, which are by definition normalized.

- [16] A. Buck, J. Wenz, J. Xu, K. Khrennikov, K. Schmid, M. Heigoldt, J. M. Mikhailova, M. Geissler, B. Shen, F. Krausz, S. Karsch, and L. Veisz, Shock-Front Injector for High-Quality Laser-Plasma Acceleration, *Physical Review Letters* **110**, 185006 (2013).
- [17] R. Lehe, M. Kirchen, I. A. Andriyash, B. B. Godfrey, and J.-L. Vay, A spectral, quasi-cylindrical and dispersion-free Particle-In-Cell algorithm, *Computer Physics Communications* **203**, 66 (2016), 1507.04790.
- [18] M. Kirchen, R. Lehe, B. B. Godfrey, I. Dornmair, S. Jalas, K. Peters, J.-L. Vay, and A. R. Maier, Stable discrete representation of relativistically drifting plasmas, *Physics of Plasmas* **23**, 100704 (2016), 1608.00215.
- [19] H. Ding, A. Döpp, M. Gilljohann, J. Götzfried, S. Schindler, L. Wildgruber, G. Cheung, S. M. Hooker, and S. Karsch, Nonlinear plasma wavelength scalings in a laser wakefield accelerator, *Physical Review E* **101**, 023209 (2020), 2001.09507.
- [20] F. Irshad, S. Karsch, and A. Döpp, Expected hypervolume improvement for simultaneous multi-objective and multi-fidelity optimization, arXiv 10.48550/arXiv.2112.13901 (2021), 2112.13901.
- [21] D. Ruppert and D. S. Matteson, *Statistics and data analysis for financial engineering*, Vol. 13 (Springer, 2011).